

Electromagnetic Source Imaging via a Data-Synthesis-Based Denoising Autoencoder

Gexin Huang, Zhu Liang Yu*, *Member, IEEE*, Ke Liu, Zheng Hui Gu, *Member, IEEE*, Feifei Qi, Yuanqing Li, *Fellow, IEEE*, Jiawen Liang, and Wei Wu*, *Senior Member, IEEE*,

Abstract—Electromagnetic source imaging (ESI) is a highly ill-posed inverse problem. To find a unique solution, traditional ESI methods impose a variety of priors which may not reflect the actual source properties. Such limitations of traditional ESI methods hinder their further applications. Inspired by deep learning approaches, a novel data-synthesized spatio-temporal denoising autoencoder method (DST-DAE) method was proposed to solve the ESI inverse problem. Unlike the traditional methods, we utilize a neural network to directly seek generalized mapping from the measured E/MEG signals to the cortical sources. A novel data synthesis strategy is employed by introducing the prior information of sources to the generated large-scale samples using the forward model of ESI. All the generated data are used to drive the neural network to automatically learn inverse mapping. To achieve better estimation performance, a denoising autoencoder (DAE) architecture with spatio-temporal feature extraction blocks is designed. Compared with the traditional methods, we show (1) that the novel deep learning approach provides an effective and easy-to-apply way to solve the ESI problem, that (2) compared to traditional methods, DST-DAE with the data synthesis strategy can better consider the characteristics of real sources than the mathematical formulation of prior assumptions, and that (3) the specifically designed architecture of DAE can not only provide a better estimation of source signals but also be robust to noise pollution. Extensive numerical experiments show that the proposed method is superior to the traditional knowledge-driven ESI methods.

Index Terms—electromagnetic source imaging (ESI), data synthesis, deep learning, denoising autoencoder (DAE)

I. INTRODUCTION

The forward problem of electro/magnetoencephalograms (E/MEGs) is defined as the transduction of cortical neuronal current activities into the potentials of scalp electrodes. In contrast, reconstructing the information about cortical activities from the scalp electrode potentials is defined as the E/MEG inverse problem, also known as the electromagnetic source imaging (ESI) problem. The solution to the ESI problem provides a detailed spatial-temporal analysis of brain activity for different functions and has broad applications in the diagnosis of brain disease [1]–[3]. However, with the limited number of

measurement electrodes compared to the unidentified sources, the ESI problem is a highly ill-posed inverse problem: there are infinite possible solutions for a given measured E/MEG signal, which poses a persisting challenge for ESI.

Regarding obtaining a unique solution, there have been numerous classical studies focusing on the prior constraints to narrow the solution space in the past decades: the minimum norm estimate (MNE) [4] is one of the classical spatially constrained methods, adopting L_2 -norm regularization to estimate the sources. Its variant named weighted MNE (wMNE) [5] improves the L_2 -norm constraint with additional weight hyperparameters. Low-resolution electromagnetic tomography (LORETA) [6] is another method based on the spatial-smooth assumption, utilizing the Laplace matrix in formulating spatial constraints. Although these methods are suitable for imaging extended sources, introducing spatial constraints incurs more diffuse estimates for focal sources [7], [8]. To avoid the diffusivity of source estimation, focal underdetermined system solution (FOCUSS) [9] and sparse source imaging (SSI) [10] introduce the sparseness regularizer based on the L_1 norm, L_p norm iterative sparse solution (LPISS) [11] proposes an iterative sparse learning algorithm based on a L_p norm, and sparse Bayesian learning (SBL) [12]–[16] utilizes the Bayesian framework with a sparsity-inducing norm. Nevertheless, these sparseness regularizers have intrinsic deficiencies in recovery of the spatial extents for extended sources and are more prone to reconstruct highly discontinuous time courses under noise pollution [17]. In addition, other studies exist that exploit various properties of neuron activity to constrain the source estimation: spatiotemporal tomographic nonnegative independent component analysis (STTONNICA) [18] decomposes the source signal into temporal and spatial components, estimating each component through a nonnegative matrix factorization model, in which hyperparameters are manually optimized to obtain a relatively good result; A few methods such as [19]–[21] exploit the physical mechanism of neural activity, the cortical tissue structure information, or other high-resolution modal information like Magnetic Resonance Imaging (MRI) into prior modeling to obtain more accurate source imaging results.

All the above traditional approaches can be classified as model-driven or knowledge-driven methods that use (mathematical, anatomical, physiological, or functional) prior assumptions to constrain the solution space of the optimization problem. Nevertheless, even though strong mathematical skills have been leveraged into the formulation of prior constraints, the constraint used in knowledge-driven model generally yield

This work was supported in part by the National Natural Science Foundation of China under Grants 61836003, 61906048, and 61703065.

Z. L. Yu, Z. Gu, Y. Li, and J. Liang are with the School of Automation Science and Engineering, South China University of Technology, Guangzhou, China, 510641. Wei. Wu is with the Department of Psychiatry and Behavioral Sciences, Stanford University, Stanford, CA, USA. K. Liu is with Chongqing Key Laboratory of Computational Intelligence, Chongqing University of Posts and Telecommunications, Chongqing, 400065, China. F. Qi is with School of Internet Finance and Information Engineering, Guangdong University of Finance, Guangzhou, 510521, China (* Corresponding author: Wei Wu. E-mail: weiwuneuro@gmail.com, Zhu Liang Yu. E-mail: zlyu@scut.edu.cn)

an approximate description of actual brain signals. A limited understanding of the underlying physical setting challenges the further expansion of knowledge-driven methods, and the numerical complexity would be greatly increased if more accurate modeling analysis is required [22]. Furthermore, the relationship between fitting the recorded data and assuring the regularization constraints should be considerably balanced by parameter tuning while solving every instance in a given problem with these methods, which is a time-consuming process and may require subjective judgement.

Since artificial neural networks can be used to find complicated mathematical maps, some prior studies utilized artificial neural network methods to solve the dipoles fitting problem [23]–[26]. But only one or two dipoles fitting can be solved due to the difficulty of optimizing the neural network. Because of the development of deep learning in recent years [27], deep neural networks can now automatically learn the mapping between inputs and outputs through large-scale training sets, in which the mapping is ultimately represented by stacked nonlinear layers. Thus, deep neural networks could be a potential new solution for the ESI problem. Recently, the source imaging framework network (SIFNet) [28] was proposed in an attempt to transform the ESI inverse problem into a supervised multiclassification task. After the brain source space is modeled as different interconnected regions, a residual-block-based classification network can be successfully trained using the generated training set, in which each training label is a one-hot vector representing the activation state of each region. However, SIFNet exploits the signal's temporal properties only in the data generation and overlooks the estimation of the temporal information of the source in inverse imaging.

In this paper, we propose a novel and efficient deep learning approach for the ESI problem that can automatically capture inverse mapping: the data-synthesized spatio-temporal denoising autoencoder (DST-DAE) method. A data synthesis strategy is proposed to generate large-scale samples of neural sources and their related scalp signals. Unlike traditional methods, the spatio-temporal properties of sources are incorporated into the generation of training signals, and no complicated mathematical modeling of prior information is required. With the advantage of universal approximation [29], the neural network is able to spontaneously learn the mapping from the measured E/MEG signals to the brain sources through the generated training set. In the network architecture, we utilize a denoising autoencoder [30] with specifically designed blocks to extract spatio-temporal features for activity localization and temporal signal reconstruction. Compared to SIFNet's classification network which focuses on the activity localization of the brain source, the proposed DST-DAE can not only locate the activated regions but also effectively reconstruct the temporal state of the source. Furthermore, the denoising process in DAE gives the proposed method robust antinoise capabilities, facilitating better handling of scalp noise pollution than that of SIFNet.

The major contributions of this paper can be summarized as follows.

- 1) A new data synthesis strategy is proposed which incorporates the spatial and temporal properties of sources

through data generation. The mathematical formulation of constraints that are always used in traditional ESI methods is avoided.

- 2) A DAE with specifically designed blocks is built that exhibits better spatio-temporal feature extraction and denoising abilities than previous autoencoders. Experiments show that the network can recover the spatial localization and temporal states of the source, even with severe noise pollution.
- 3) A deep learning enhancing source imaging algorithm is proposed that can easily be implemented with three phases. Experiments show that better performance than that of traditional knowledge-driven algorithms can be achieved.

The remainder of the paper is organized as follows. The proposed DST-DAE approach is introduced in Section II. Section III presents the experimental results on simulated and real datasets. Some discussion about the merits and drawbacks of DST-DAE is presented in Section IV. Finally, a brief conclusion is given in Section V.

II. METHODOLOGY

A. Electromagnetic Source Imaging Problem

The electrical activity of nerve inside the brain generates electrical/magnetic signals, which pass through the internal tissues of the head and can be recorded by electrodes on the scalp [2]. The ESI problem is the determination of the source activities through the measured E/MEG signals. Therefore, accurately establishing the head volume conduction model is one of the crucial premises of the ESI problem.

The forward model of the E/MEG signal is given as

$$\mathbf{X} = \mathbf{L}\mathbf{S} + \boldsymbol{\varepsilon}, \quad (1)$$

where $\mathbf{X} = [\mathbf{x}_1, \dots, \mathbf{x}_t, \dots, \mathbf{x}_T] \in \mathbb{R}^{N_c \times T}$ represents the matrix of the measured EEG signals and column $\mathbf{x}_t = [x_{1t}, \dots, x_{N_c t}]^T$ represents the recorded signal vectors at time t from N_c electrodes. $\mathbf{S} = [\mathbf{s}_1, \dots, \mathbf{s}_t, \dots, \mathbf{s}_T] \in \mathbb{R}^{N_s \times T}$ is the matrix of the unknown source signals, and column $\mathbf{s}_t = [s_{1t}, \dots, s_{N_s t}]^T$ represents the source signal vectors at time t from N_s sources. $\boldsymbol{\varepsilon} \in \mathbb{R}^{N_c \times T}$ denotes the measurement noise. The matrix \mathbf{L} is the transfer matrix (also called the lead field matrix), which represents the relationship from a unit source at a certain location to the measured E/MEG signals. It can be obtained by numerical methods such as the finite element model (FEM) [31] and boundary element model (BEM) [32] from CT/MRI scanning of the human head.

The ESI problem aims to find a projection $P_\theta(\cdot)$ from E/MEG signals \mathbf{X} to source signals \mathbf{S} with the prior known lead field matrix \mathbf{L} as :

$$\mathbf{X} \xrightarrow{P_\theta(\cdot)} \mathbf{S}. \quad (2)$$

As N_c is far less than N_s , the ESI problem is an under-determined inverse problem. In traditional methods, it can be solved by utilizing regularization techniques, obtaining a proper solution \mathbf{S}^* as follows:

$$\mathbf{S}^* = \arg \min_{\mathbf{S}} D(\mathbf{X}, \mathbf{S}) + R(\mathbf{S}), \quad (3)$$

where $D(\mathbf{X}, \mathbf{S})$ represents the data discrepancies between the original scalp signals and the reconstruction signals calculated by the estimated source signals and the $R(\mathbf{S})$ is the regularization term of the source. Some prior knowledge of the source is formulated as constraints and merged into $R(\mathbf{S})$. An optimal \mathbf{S}^* is finally obtained by explicit mathematical optimization. Some challenges in this problem are as follows: 1) attribute to the challenges in formulating constraints and the difficulties in solving analytical models, traditional methods have to introduce approximate assumptions for $R(\mathbf{S})$; 2) the process of optimizing \mathbf{S}^* needs to rigidly guarantee its convergence and stability in mathematics [19].

With the existence of the lead field matrix obtained by forward modeling, in this paper, we proposed a new method based on a data-synthesized deep learning strategy to solve the ill-posed ESI problem.

B. Data-Synthesized Deep Learning Strategy

The proposed method aims to utilize a nonlinear neural network to fit the mapping $P_\theta(\cdot)$, where θ represents its parameters. As a prerequisite, the network should have enough source and E/MEG data samples for the networks training. However, a major problem in practice is that these data samples are hardly acquired. With the lead field matrix, large-scale samples of sources and E/MEG signals can be generated. This renders an end-to-end neural network feasible and converts the ill-posed inverse problem into a multi-target linear regression problem. Consequently, two questions are of our focus: 1) how to synthesize realistic data for model training; 2) how to build a proper neural network architecture to enable the estimation of the multi-target linear regression model. In this paper, to better reflect the spatio-temporal properties of the source signals, we utilize the prior information on the smoothness of their time courses and the anatomy of the head tissues for the data synthesis. These properties encoded in the synthesized data can then be effectively learned by training the neural network, whose specific architecture will be illustrated in Section II-C.

The general idea of DST-DAE is shown in Fig. 1. First, we decompose the source data into temporal and spatial components and introduce corresponding prior knowledge to form their corresponding prior space. Then, various spatial and temporal states are generated by uniformly sampling from those spaces. After that, the generated source signal, denoted as \mathbf{S}_g , is obtained by convoluting the temporal signals with the source active states, and the corresponding scalp signal, denoted as \mathbf{X}_g , can be simulated through the forward process. Thus, a large-scale dataset about the source and scalp signals in various states can be generated. Then, the dataset is used as a training set from which the neural network can extract a proper mapping pattern. Through the minimization of the loss function $\mathcal{L}_\theta(\cdot)$ for training the neural network, the optimal parameters can be acquired as $\theta^* = \arg \min_\theta \mathcal{L}_\theta(\mathbf{X}_g, \mathbf{S}_g)$. Finally, inverse mapping $P_{\theta^*}(\cdot)$ can then be used for inverse imaging. More specific implementation details are explained in Section II-D.

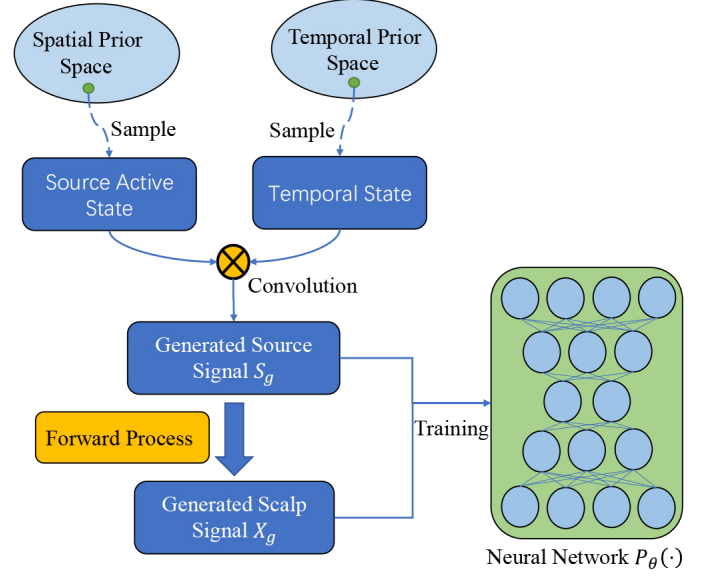


Fig. 1: General idea of the data-synthesized deep learning strategy for the ESI problem.

C. Design of the Neural Network

E/MEG signals have a low signal-to-noise ratio (SNR) and low spatial resolution. High-noise E/MEG samples make network training more difficult and affect the source reconstruction performance. Therefore, the DAE architecture is proposed for our network. The DAE is robust against scalp noise pollution via training. Besides, its bottleneck structure can not only extract the principal features through dimensionality reduction but also reduce the complexity of the numerical calculation due to the fewer network parameters. To better extract the spatio-temporal features of E/MEG signals, inspired by the EEG decoding network [33]–[35], we design the blocks with spatio-temporal stepwise convolution/deconvolution in our neural network.

1) *Overall Structure of the Neural Network:* The overall network structure is shown in Fig. 2(a). The generated E/MEG signals \mathbf{X}_g and the corresponding generated source signals \mathbf{S}_g are input into the neural network as training samples, and \mathbf{X}_n is the noise corrupted version of \mathbf{X}_g . In the encoder, there are two feature extraction blocks: temporal and spatial encoding blocks. First, the principal temporal feature \mathbf{X}_t is extracted from the noise corrupted E/MEG signals through the temporal encoding block. Then, the spatio-temporal principal feature \mathbf{X}_{st} is consequently obtained through the spatial encoding block. In the decoder, which has spatial and temporal decoding blocks, \mathbf{X}_{st} is firstly decoded as the source temporal feature \mathbf{S}_t through the spatial decoding block. Then, \mathbf{S}_t is further temporally decoded for the reconstruction of the source \mathbf{S}_{re} through the temporal blocks. Finally, as the output of the network, the reconstructed scalp signal \mathbf{X}_{re} is calculated using the forward model. In contrast to a traditional DAE, we separately measure the data discrepancies of \mathbf{S}_{re} and \mathbf{S}_g , and of \mathbf{X}_{re} and \mathbf{X}_g , as shown by the two ends of the dotted line in Fig. 2, considering their weighted sum as the overall loss function.

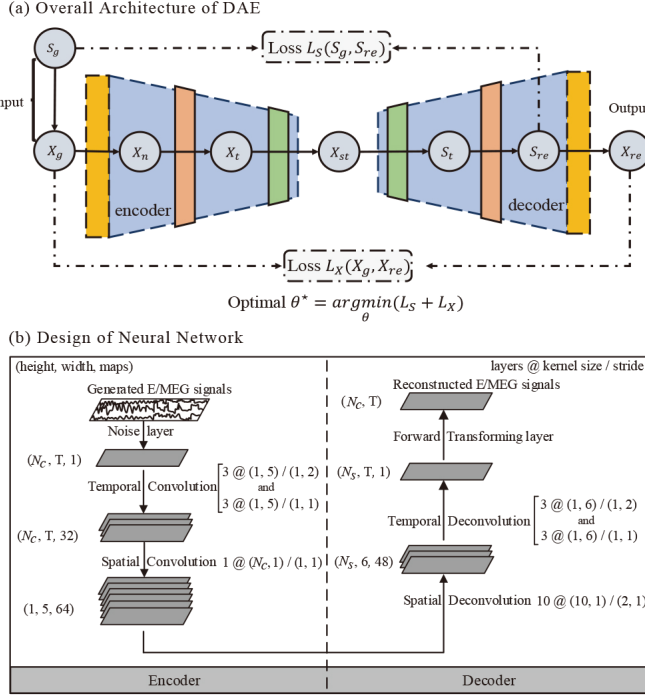


Fig. 2: Overall architecture and detail of the DAE. (a) The overall architecture. The arrowed lines indicate the input-to-output sequence of the DAE, and the two dashed lines represent the related tensors for calculating the corresponding loss function. (b) Detailed setting of the neural network. N_c and N_s separately represent the number of electrodes and sources. T is the time sampling point of the signals. In our experiments, we downsampled the time points to 40.

2) *Encoder and Decoder*: The details of the neural network are exhibited in Fig. 2(b). The network can be divided into 6 layers as follows:

Noise block \mathfrak{N} ($\mathbb{R}^{N_c \times T} \rightarrow \mathbb{R}^{N_c \times T}$): This block contains a generation process of white Gaussian noise and uses the generated noises to corrupt X_g into X_n with the specified SNR. This block is only used during the period of DAE training.

Temporal encoding block \mathfrak{h} ($\mathbb{R}^{N_c \times T} \rightarrow \mathbb{R}^{N_c \times K_t \times F_1}$): This block contains multiple stacks of 2-D convolutional layers with a convolution kernel of 1×5 and a step size of 1×2 . It independently implements temporal convolution on each electrode channel. This block extracts the principal temporal feature $X_t = \mathfrak{h}(X_n)$ with F_1 temporal feature maps. For each feature map, the temporal size is compressed from T into K_t points.

Spatial encoding block \mathfrak{g} ($\mathbb{R}^{N_c \times K_t \times F_1} \rightarrow \mathbb{R}^{1 \times K_t \times K_s}$): This block contains a 2-D convolutional layer with a convolution kernel of $N_c \times 1$ and a step size of 1×1 . It separately implements a full-spatial convolution on each temporal channel and extracts the spatio-temporal feature $X_{st} = (X_t)$ with the $K_s \times K_t$ spatio-temporal feature maps.

Spatial decoding block \mathfrak{g}^{-1} ($\mathbb{R}^{1 \times K_t \times K_s} \rightarrow \mathbb{R}^{N_s \times K_t \times F_2}$): This block contains multiple stacks of 2-D deconvolutional layers with a kernel size of 10×1 and a step size of 2×1 . It

decodes X_{st} to the source temporal feature $S_t = \mathfrak{g}^{-1}(X_{st})$ with F_2 deconvolutional feature maps. Each feature map has a $N_s \times K_t$ source temporal feature map.

Temporal decoding block \mathfrak{h}^{-1} ($\mathbb{R}^{N_s \times K_t \times F_2} \rightarrow \mathbb{R}^{N_s \times T}$): This block contains multiple 2-D deconvolutional layers with a kernel size of 1×6 and a step size of 1×2 . We set the kernel size of the deconvolutional layer to even number 6 to avoid checkerboard artifacts [36]. This block further decodes S_t to estimate the reconstructed source signal $S_{re} = \mathfrak{h}^{-1}(S_t)$.

Forward transformation block \mathfrak{f} ($\mathbb{R}^{N_s \times T} \rightarrow \mathbb{R}^{N_c \times T}$): This block calculates the reconstructed scalp signal through the lead field matrix: $X_{re} = \mathbf{L}S_{re}$. The introduction of X_{re} in network training can efficiently improve the training performance.

To accelerate network training, the exponential linear units (*elu*) function [37] is utilized as the activation functions for all convolution and deconvolution layers except for the last deconvolutional layer before S_t , for which a linear activation function is used. Furthermore, because of the tremendous diversity among the generated samples, a large-scale-training strategy for parameter initialization is difficult to implement. In addition, because of the oscillating training loss induced by data diversity, the network cannot easily convergence. Therefore, a Batch Normalization (BN) layer, as suggested in [38], is added between the deconv/convolutional layer and the activation layer. This can prevent the distribution shift and effectively eliminate the variance drift induced by feature transformation, which is desirable because shift and drift lead to weight saturation and further decelerated learning. After our experimental testing, the network with the BN layer is not only insensitive to the parameter initialization on each layer but also converges quickly and smoothly.

3) *Loss Function*: In this paper, two error functions, the data-discrepancy function of measurements $D(X_g, S_g)$ and the auxiliary regularization-like function of source $\bar{R}(S_g)$, are proposed, and the final loss function is the weighted sum of these functions.

$$\begin{aligned} \mathcal{L}_{\theta}(X_g, S_g) &= \lambda_1 D(X_g, S_g) + \lambda_2 \bar{R}(S_g) \\ &= \lambda_1 \mathcal{L}_X(X_g, X_{re}) + \lambda_2 \mathcal{L}_S(S_g, S_{re}) \end{aligned} \quad (4)$$

where $\lambda_1 \geq 0$ and $\lambda_2 \geq 0$ are loss weights and

$$\mathcal{L}_X(X_g, X_{re}) = \frac{1}{N} \sum_i \|X_g^{(i)} - X_{re}^{(i)}\|_{\mathcal{F}}^2, \quad (5)$$

$$\mathcal{L}_S(S_g, S_{re}) = \frac{1}{N} \sum_i \left[\|S_g^{(i)} - S_{re}^{(i)}\|_{\mathcal{F}}^2 + \delta \|S_g^{(i)} - S_{re}^{(i)}\|_{1,1} \right], \quad (6)$$

where N represents the total number of training sets and $\delta \geq 0$ is a manually set parameter. The loss weight is further discussed in Section III-F.

The mean square error (MSE) is more sensitive to high amplitude errors, while the mean absolute error (MAE) can be equally sensitive to minor differences. First, to facilitate a highly precise reconstruction of sources by the network, we used the weighted sum of the MSE and MAE as a regularization-like function for the source. Second, due to the

existence of scalp noise, excessively pursuing reconstruction consistency for scalp signals leads to overfitting. To prevent this situation, only the MSE was used for the measurement of the data discrepancy of the scalp signals.

In contrast to the traditional methods, the optimization process of DST-DAE implicitly exploits prior knowledge of the source. In the loss function, $R(S)$ is generally a prior constraint of the source in the traditional methods, while $\bar{R}(S)$ is the data discrepancy between the reconstructed and generated sources. As the generated data contain the prior knowledge of the source, minimizing the source discrepancy indirectly allows the network to learn the prior knowledge. Thus, we can easily utilize the prior information without complex mathematical modeling. A comparison of the performance of different ESI algorithms is presented in Section sections III-B to III-E to further illustrate the advantages of DST-DAE.

D. Implementation Process of Algorithm

The application of DST-DAE includes three phases: the data synthesis phase, the training phase and the estimation phase.

1) *Data Synthesis Phase*: To better utilize the spatio-temporal characteristics of E/MEG signals, we adopt the spatial and temporal information in the generation of source signals:

$$\mathbf{S}_g = \mathbf{W}\Phi = \sum_{k=1}^K \mathbf{w}_k \phi_k, \quad (7)$$

where $\Phi \in \mathbb{R}^{K \times T}$ is the temporal state matrix and $\mathbf{W} \in \mathbb{R}^{N_s \times K}$ represents the activation state matrix of the brain source space with K spatial principal components. ϕ_k is the k -th temporal information component generated from a set of temporal basis functions (TBFs) $\Theta \in \mathbb{R}^{m \times T}$ with m components. \mathbf{w}_k is the k -th spatial principal component:

$$\mathbf{w}_k = \begin{cases} 1 & s_i \in \gamma \\ 0 & \text{else} \end{cases}, \quad (8)$$

where s_i represents the i -th vertex of the source and γ represents the index set of activated sources.

To achieve large-scale training, we generate a large number of spatial activation states \mathbf{W} and temporal states Φ . For the i -th generated sample, first, we sample from a uniform distribution to randomly obtain the seed source s_{seed} in the source activity space. The index set is obtained by generating activated sources whose total area of them is subject to a given value A within the seed's neighborhood n : $\gamma^{(i)} = \{s_j | \text{area}(\gamma) = A, s_j \in n(s_{seed})\}$, where A is uniformly sampled under a maximum area a_{max} chosen according to the prior knowledge.

Second, we use methods such as the stimulus evoked factor analysis (SEFA) [39] or singular value decomposition (SVD) [40] to estimate the TBFs from the real scalp signal X_{real} . Then, $\phi_k^{(i)}$ is generated from the subspace spanned by the basis Θ as $\phi_k^{(i)} = \sum_{m=1}^M \zeta_m^{(i)} \Theta(m)$, where weight $\zeta_m^{(i)}$ is obtained from uniform sampling.

Finally, the i -th generated source signal $\mathbf{S}_g^{(i)}$ can be obtained by convoluting the spatial activation state $\mathbf{W}^{(i)}$ with the

temporal state $\Phi^{(i)}$, and the corresponding generated scalp signal $\mathbf{X}_g^{(i)}$ can be calculated by the forward model with the known lead field matrix \mathbf{L} .

2) *Training Phase*: We engage the generated dataset $(\mathbf{S}_g, \mathbf{X}_g)$ as the training set for the neural network. First, the scalp SNR is estimated through the prestimulus stage of \mathbf{X}_{real} and is set as the noise level of the noise block to corrupt $\mathbf{X}_g^{(i)}$. After that, through the minimization of the loss function until the loss value converge, the neural network is trained and automatically learns the mapping from the scalp to the source.

3) *Estimation Phase*: In this phase, the noise block is deactivated. Only the blocks of the trained neural network from \mathbf{X}_n to \mathbf{S}_{re} are used to reconstruct the source signals. The real scalp signal \mathbf{X}_{real} is mapped to the optimal source signal \mathbf{S}^* by the trained network.

III. EXPERIMENTS

In this section, first, some experiments were carried out to compare the performance of the proposed method to that of several model-driven methods, including two L_2 -norm methods, wMNE [5] and LORETA [6], which were proposed for the reconstruction of spatial extents source, two sparse-constrained methods, SBL [13] and FOCUSS [9], which are superior for estimating point sources; and a spatio-temporal constrained method, STTONNICA [18], which also decomposed source into spatial and temporal components and optimized under Bayesian information criterion (BIC) in estimation. The performance of DST-DAE is assessed by evaluating recovered source images and performance metrics under different conditions. Second, two experiments on the training setting of the neural network were proposed to further illustrate the characteristics of DST-DAE. Finally, an experiment on real MEG data was conducted to illustrate that DST-DAE can achieve better performance than the other algorithms in practice.

A. Experimental Design and Performance Metrics

1) *Protocol of Simulation Experiments*: In the following experiments, using Brainvisa¹, the brain cortical surface was obtained by segmenting the white/gray matter interface of default MR images derived from MNI/ICBM152 in Brainstorm [41]. Then, the cortical mesh was downsampled to a total of 1024 triangular elements and was utilized to build the source space. The sensor template was configured as the 65-channel Neuroscan Quikcap system. The lead field matrix \mathbf{L} was computed through the BEM method. This process was implemented in the OpenMEEG plug-in [42] in Brainstorm. In the preprocessing, 2 reference electrodes were removed, and the corresponding row vectors in \mathbf{L} were consequently removed.

The time course of each patch source was simulated as a Gaussian damped sinusoidal time course formulated as: $\sin(2\pi f) \exp^{-(t-\tau/\omega)^2}$. Through the choice of different f , ω , and τ , event-related potential (ERP) signals with various temporal states could be simulated. A source activity region

¹<http://www.brainvisa.info>.

was simulated by first selecting a triangular element on the cortical mesh as a seed voxel in the regional center and second enlarging the region by iteratively absorbing its neighbor elements until the required area condition was achieved. The source signals could be constructed by placing the simulated ERP signals at the source active regions, and the corresponding EEG signals were calculated by the forward model. White Gaussian noise with a specific SNR was added to the simulated signals. The SNR was defined as $SNR = 10 \log_{10} \frac{\|LS\|_F^2}{\|\varepsilon\|_F^2}$. In our simulation experiments, we generated the ERP signal with 40 sampling points per trial, and the relative TBF basis was obtained by SEFA. Without loss of generality, we give the TBF basis 4 different principal components.

In simulation experiments, we designed four scenarios to explore the merits and shortcomings of DST-DAE compared to the other classical methods mentioned above:

- Single active patch source with varying SNRs: we kept the source area at $5 \pm 0.58 \text{ cm}^2$ and set the SNR to -5 dB, 0 dB, 5 dB, and 10 dB.
- Single active patch source with varying spatial extents: we kept the SNR at -5 dB and set the source area to 3 cm^2 , 6 cm^2 , 10 cm^2 , and 15 cm^2 .
- Two patch sources with varying spatial patterns: we kept the SNR at -5 dB and set the source pattern to 4 cm^2 and 4 cm^2 , 4 cm^2 and 10 cm^2 , 10 cm^2 and 4 cm^2 , and 10 cm^2 and 10 cm^2 .
- Two patch sources with varying correlated sources: we kept SNR at -5 dB and fixed the source areas at 7 cm^2 ; then, we set the coefficient correlation of the correlated source signals to 0, 0.3, 0.6, and 0.9.

Without loss of generality, we set $a_{max} = 20$ in the training phase. This indicates that the generation threshold of the source activation is between 0 cm^2 and 20 cm^2 . The simulated data were normalized before training to improve the numerical stability. Then, for each condition mentioned above, 100 Monte Carlo numerical simulations were implemented to test the reconstruction performance.

2) *Parameter Setting*: The network was implemented in Python with Keras library using TensorFlow Backend. MATLAB and Brainstorm toolbox was used for data processing. We chose Adam, which is a gradient descent algorithm, as the optimizer, and the hyperparameters were set as follows:

First, we set $K_t = 5$ and $K_s = 64$ for the spatio-temporal principal feature X_{st} . The learning rate of the Adam optimizer was set to 10^{-4} , and the other hyperparameters of the Adam optimizer were set to the values suggested in [43] of $\beta_1 = 0.9$, $\beta_2 = 0.999$ and $\epsilon = 10^{-8}$. We set the batch size to 32 for the mini-batch stochastic gradient descent, and all the trainable parameters in the neural network were initialized with the Glorot Uniform method. The numbers of iterations of the deep learning model training was set to 200-300. We gave every convolutional and transpose-convolutional layer a weight decay strategy by setting L_1 and L_2 regularizers. The setting parameter δ was set as 0.1.

To further improve the performance of the proposed DST-DAE, we utilized a warm-up strategy [44] to dynamically fine-tune the learning rate during the training. We set the learning

rate to linearly increase to a maximum in the first 20 epochs and linearly decrease to a minimum in the last 20 epochs.

3) *Performance Metrics*: In simulation experiments, the performance of all the ESI methods was assessed with the four metrics:

- The area under the receiver operating characteristic curve (AUC): evaluates the sensitivity and specificity of the source detection.
- The relative mean square error (RMSE): evaluates the accuracy of the reconstructed time courses.
- The distance of localization error (DLE): measures the localization error through the average distance from the activity peak of the estimated sources to those of the true ones.
- The spatial dispersion (SD): measures the extent to which the estimated sources are spatially blurred.

The utilization of multiple metrics allows us to more comprehensively evaluate the performance of each method. In general, we hope that the performance of the advanced method has a relatively high AUC value and relatively small RMSE, SD, and DLE values.

Furthermore, we utilized the R-square (R^2) [45] score function for the source signals as an indicator of the training performance of the network. A larger R^2 value, with an optimal value of 1, illustrates a better fitting ability of a nonlinear network. The source maps are thresholded using Otsu's method [46]. The details of each metrics and Otsu's method are presented in supplementary materials.

B. Experiment I: Single Patch Source with Varying SNRs

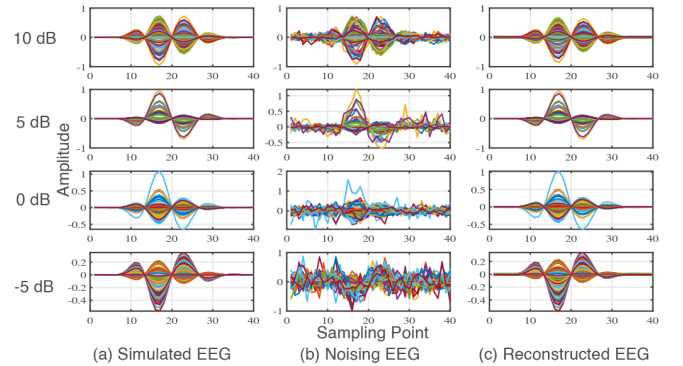


Fig. 3: Results of the denoising ability of the DAE for EEG signals with varying SNRs. The left column represents EEG signals without noise randomly sampled from each group of test samples. The middle column represents the corresponding noisy signals. The right column represents the reconstructed signals that are denoised via the neural network.

In the first experiment, we evaluate the performance of signal reconstruction for brain source and scalp EEG with varying SNRs. As shown in Fig. 3, and Table I, it is clear that the proposed DAE can reconstruct the principal temporal information of EEG signals even with severe noise pollution.

Fig. 4 presents the aforementioned performance metrics for 100 Monte Carlo simulations. Regarding the AUC value,

SNR (dB)	-5	0	5	10
RMSE	0.781±0.036	0.519±0.029	0.269±0.015	0.132±0.005

TABLE I: RMSE values between the simulated EEG signals and reconstructed signals. The mean and standard deviation are calculated by 100 Monte Carlo simulations per scenario.

the performance of wMNE and LORETA worsens as the noise increases, while STTONNICA, SBL, and FOCUSS are relatively robust to varying noise. It is clear that the AUC value of DST-DAE is higher than that of the others and steadily varies. Thus, the reconstruction performance of DST-DAE is robust to different levels of noise. As an increase in noise enhances the diversity in training samples, the generalization performance of the neural network relatively benefits from increasing noise. Therefore, the AUC of DST-DAE slightly declines at 10 dB SNR. Additionally, the RMSE values of all the algorithms deteriorate with the increase of noise. DST-DAE has the smallest RMSE and its degree of decline is relatively mild. Furthermore, DST-DAE achieves lower DLE and SD values along with the sparse constrained methods such as SBL or FOCUSS, but the latter is due to their reconstruction of focal sources.

A comparison of the source imaging performance is shown in Fig. 5. Under different SNRs, the reconstructed sources of the L_2 -norm based methods, wMNE or LORETA, are more diffuse, and this phenomenon worsens as the noise increases. The sparse constrained methods, SBL and FOCUSS, reconstruct the patch sources into focal sources and generate spurious sources as the noise increases. After the hyperparameters are carefully set, STTONNICA can locate relatively compact brain sources. The proposed DST-DAE can reconstruct a more accurate spatial extent. The intrinsic reason is that DST-DAE incorporates prior information through data generation and learns this knowledge during antinnoise training. Compared to the manually regularized methods, DST-DAE can automatically exploit the source characteristics in imaging. Therefore, all the indicators and source images demonstrate that DST-DAE yields a more robust antinnoise performance than the other traditional algorithms.

C. Experiment II: Single Patch Source with Varying Spatial Extents

Next, we further explored the performance of DST-DAE for a single patch source with different spatial extents under -5 dB SNR. Similarly, we analyzed the performance metrics as shown in Fig. 6. It is clear that DST-DAE achieves the highest AUC value and the smallest RMSE value under different conditions, and these indicators change relatively smoothly as the conditions vary. Furthermore, DST-DAE still achieves relatively small SD and DLE values, which demonstrates that DST-DAE can recover a source with less spatial diffusion and a more accurate location.

The results for the source imaging are shown in Fig. 7. It is clear that SBL and FOCUSS tend to reconstruct the focal source no matter how large the spatial extents, while the reconstruction sources of wMNE and LORETA are too

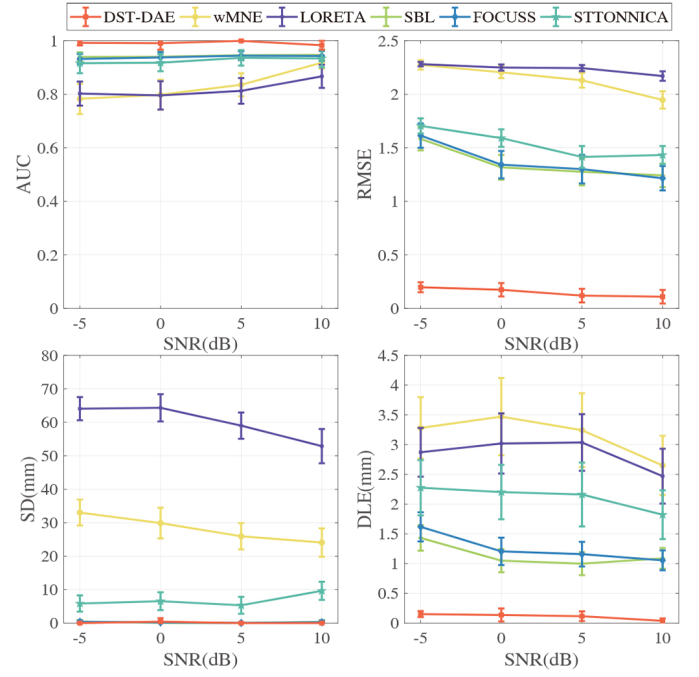


Fig. 4: Performance metrics with varying SNRs. The figure shows the results of 100 Monte Carlo simulations, and the data are shown as the Mean \pm SEM (SEM: standard error of the mean). There are four metric indicators: 1) the AUC evaluates the sensitivity and specificity of the source localization, 2) the RMSE evaluates the accuracy of the reconstructed time courses, 3) the SD measures the spatial blurred extent, 4) the DLE depicts the localization error.

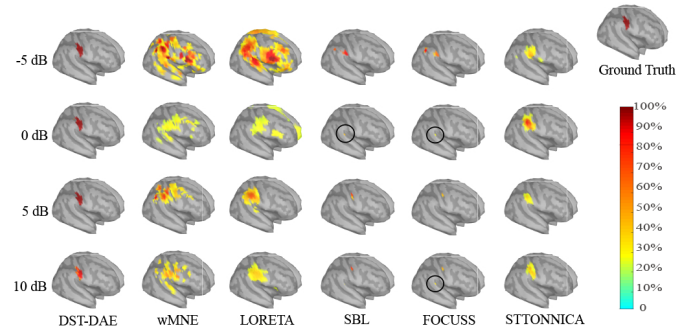


Fig. 5: Source estimates with varying SNRs. The results are presented as the absolute values of the current activities at the peak of the simulated sources and threshold using Otsu's method. The areas of the sources are all 5 cm^2 .

diffuse, as they favor spatially blurred solutions. STTONNICA can relatively accurately estimate the source location, but the spatial extents are still imprecise due to its strict prior constraints. Benefitting from the diverse source states in training data, DST-DAE can still estimate accurate spatial extents. In summary, DST-DAE achieves a better performance than the traditional algorithms for different spatial extents.

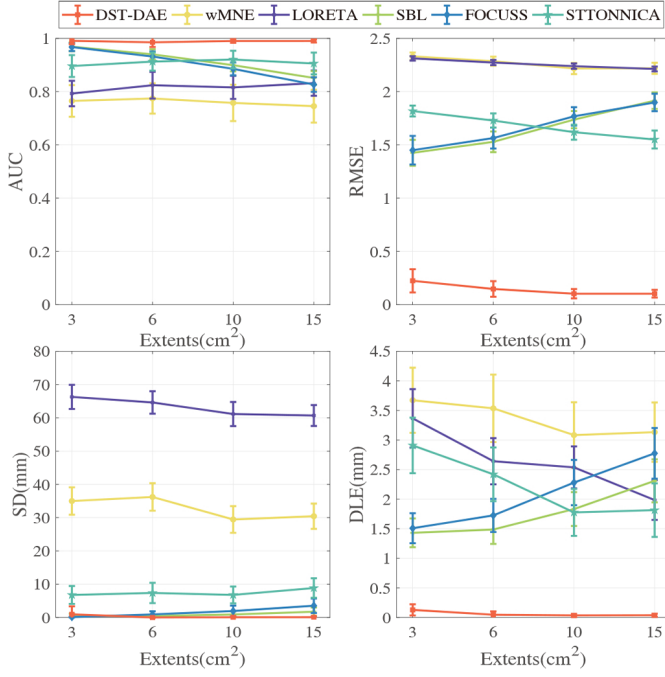


Fig. 6: Performance metrics with varying spatial extents. The figure shows the results of 100 Monte Carlo simulations, and the data are shown as the Mean \pm SEM. The SNR is -5 dB.

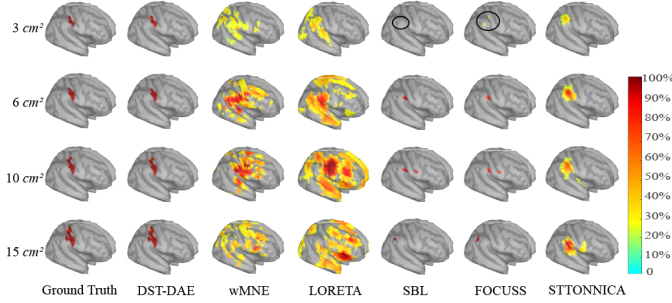


Fig. 7: Source estimates with varying spatial extents. The results are presented as the absolute value of the current density at the peak and threshold using Otsu's method.

D. Experiment III: Two Patch Sources with Varying Spatial Patterns

To further investigate the abilities of DST-DAE on practical problems, we evaluated the ESI performance under multiple sources. Without loss of generality, we assumed that the source space is activated by two different sources, in which each source supplies different ERP signals.

In the analysis of the performance metrics (Fig. 8.), it is clear that DST-DAE achieves lower SD and the smallest DLE compared to those of wMNE, LORETA, and STTONNICA. Even though the AUC values of all the algorithms degrade to a certain extent, DST-DAE still achieves the highest AUC value and the smallest RMSE value. Thus, DST-DAE is capable of locating an accurate source extent and is superior for the reconstruction of the temporal information of a source.

A comparison of the source imaging performance is exhibited in Fig. 9, which shows that the location accuracy of all

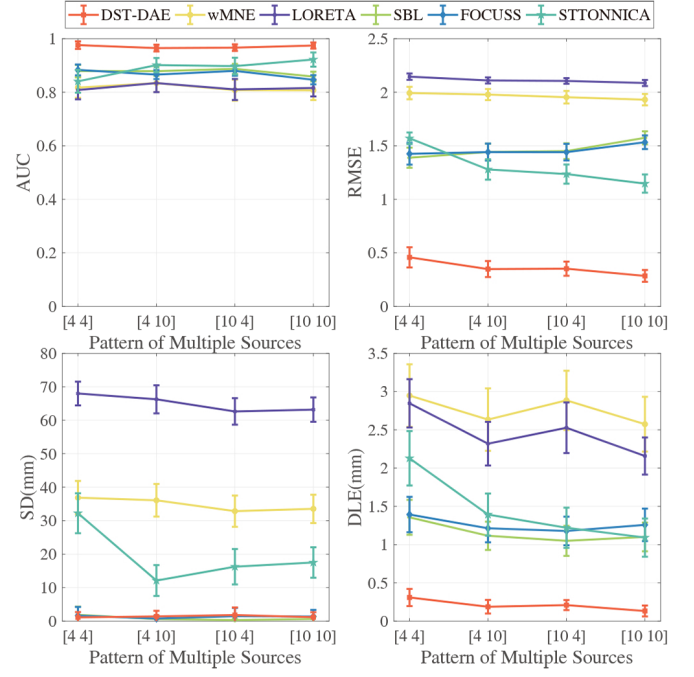


Fig. 8: Performance metrics for two patch sources with varying spatial patterns. The x-axis represents different patterns of multiple sources, in which the number indicates the area for each source. The figure shows the results of 100 Monte Carlo simulations, and the data are shown as the Mean \pm SEM. The SNR is -5 dB.

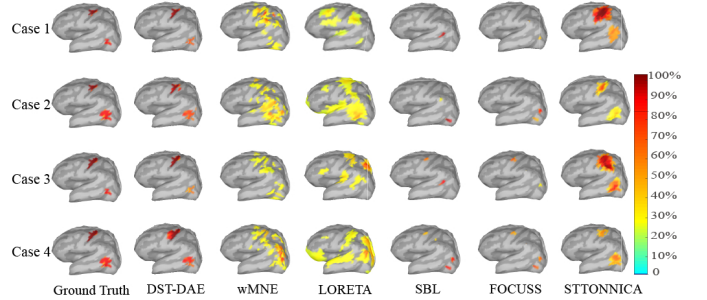


Fig. 9: Source estimates for two patch sources with varying spatial patterns. The results are presented as the absolute value of the current density at the peak and threshold using Otsu's method.

the algorithms decreases under multiple sources. The source estimations of wMNE or LORETA are still diffuse, while those of SBL or FOCUSS include a large number of spurious sources. STTONNICA obtains a relatively compact source by manually searching the parameters, but the recovery of the spatial extent is still not good enough compared to DST-DAE. Overall, DST-DAE still achieves performance superior to that of the other traditional algorithms under multiple sources.

E. Experiment IV: Two Patch Sources with Varying Correlated sources

Furthermore, to explore the temporal reconstruction ability of DST-DAE under multiple sources, we designed 4 groups

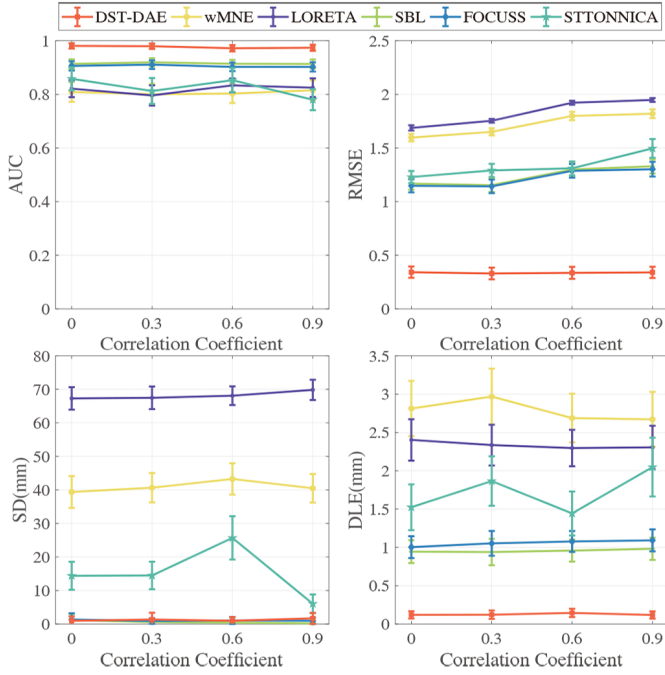


Fig. 10: Performance metrics with varying correlated sources. The figure shows the results of 100 Monte Carlo simulations, and the data are shown as the Mean \pm SEM. The SNR is -5 dB. The areas of the sources are all 7 cm^2 .

of simulation sets with different correlated sources for the experiment. As shown in Fig. 10, DST-DAE still has the highest AUC value. Moreover, DST-DAE has a stable and minimal RMSE value under varying correlated sources, while the RMSE values of the traditional methods increase with increasing correlation. This demonstrates that model-driven methods have difficulty differentiating similar temporal states. According to the SD and DLE indicators, SBL, FOCUSS, or STTONNICA are relatively sensitive to the temporal state. STTONNICA performs the worst among them, showing drastic fluctuation for highly correlated sources. In contrast, DST-DAE achieves small SD and DLE values.

Fig. 11 further shows a comparison of the temporal information reconstructions for each group. We separately selected the corresponding center source from two correlated sources as a reference for comparison with the temporal reconstruction of the different methods. wMNE and LORETA can identify the activated states of the source, but the temporal states fluctuate more. SBL or FOCUSS can clearly identify the peak of the activated source but tend to miss one of the two sources with the increasing correlation. STTONNICA can recover a relatively smooth waveform due to its model assumptions but cannot differentiate temporal information well for highly correlated sources. It is clear that the proposed DST-DAE can generally reconstruct more accurate temporal information through the same neural network.

F. Sensitivity Analysis for the Loss Weight

In this section, we conducted a sensitivity analysis for the two-part weights of the loss function. We separately fixed each

weight and changed another weight to train the network in fixed 9000 training samples. The corresponding changes for the R^2 performance of the network are separately recorded. According to our experimental fine-tuning, the optimal loss weights are $\lambda_1 = 10$ and $\lambda_2 = 150$. Because uniformly scaling the scalar amplitude does not influence the training performance, we separately normalized each loss weight into $[0, 1]$ in the experiment for a better illustration. In the first experiment, we set λ_2 to the scaled optimal value, as $\frac{1}{15}$, and adopted a grid-search to obtain 40 equally spaced λ_1 parameters between 0 and 1. The opposite operation is implemented in the second experiment. The experimental results are shown in Fig. 12. First, it is clear that the performance of the neural network is positively correlated with both loss weights. Second, with increasing loss weight, there exists a discontinuous change for R^2 metric due to its nonlinear transformation. Assuming that the loss weight of a certain part is 0, which means its loss function is not added, the performance of the network sharply degraded. This proves that the loss functions of both parts are necessary for training DST-DAE. Finally, since the performance of the network saturates as the loss weight increases, the performance limit is not determined by the loss weight but by the network architecture.

G. Performance of the Neural Network with Various Generated Training Set Scales

Training Sample	1500	4500	9000	18000	27000	36000
R^2	0.253	0.448	0.686	0.856	0.913	0.922

TABLE II: Results for the R^2 metric of the source signals with various training set scales. R^2 is measured with the simulated and estimated source signals in the test set.

To explore the effect of the sample size on network training, we trained the network with various training data scales under a single patch source condition. In Fig. 13, we exhibit the transformation of the training and validation loss with various data scales. It is clear that the losses of the training and validation set gradually decrease as the sample size increases and that the overfitting phenomenon gradually diminishes. Tab. II shows the transformation of the R^2 indicator with the various test set scales. As shown, R^2 gradually increases as the sample size enlarges, indicating that the network accuracy of estimating the source information is increasing. However, the improvement of R^2 gradually slows down and finally converges. This demonstrates that simply augmenting the scale of training data could not infinitely improve the reconstruction performance, even though the performance is related to the scale.

H. Real MEG Experiment

The MEG median nerve data are from a stimulation experiment on the left and right thumb, and include 301 left-hand experiments and 302 right-hand experiments. The experiment was performed by Massachusetts General Hospital recording through the Neuromag Vectorview 306 system. The MEG

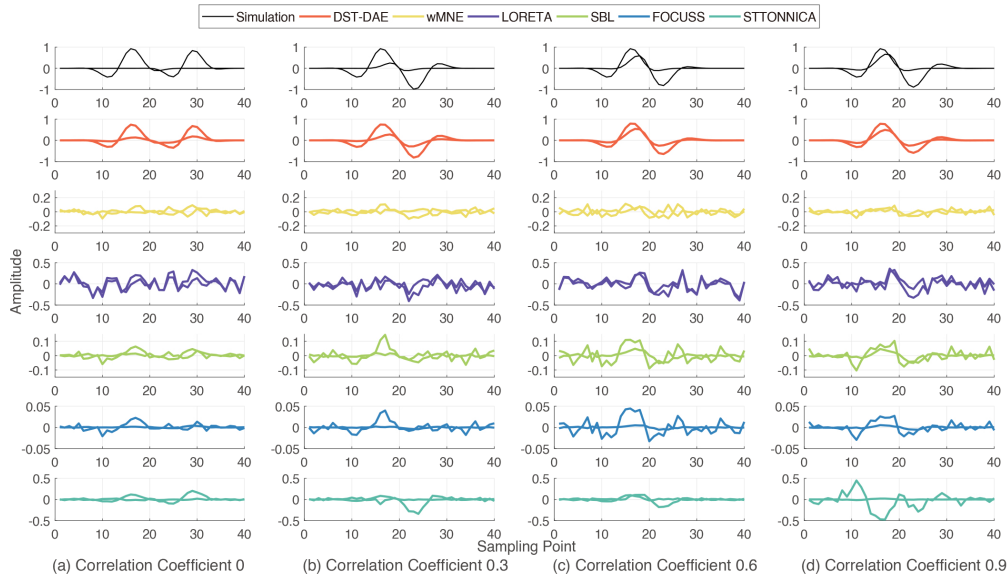


Fig. 11: Reconstruction of the temporal courses with varying correlated sources. We separately selected the corresponding center source from two correlated sources as a reference for comparison with the temporal course estimates of the different methods. The two center sources had different correlated temporal states in each case. To better exhibit reconstruction details, we modified the range of the corresponding y-axis to adapt to each algorithm. The SNR is -5 dB.

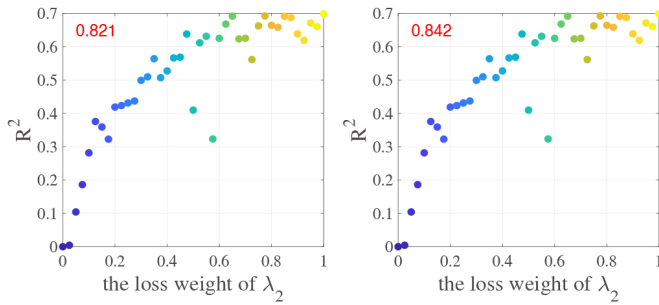


Fig. 12: Results for the R^2 metric of source signals with different weight losses. In each scenario, each weight of them has been fixed separately, and its counterpart is set to 40 equally spaced values via grid-search. The number of training samples is 9000. R^2 metric is measured by simulated and estimated source signals in validation set. The numbers in the upper-left are the correlation coefficients of the R^2 metric and weight.

dataset can be downloaded from the Brainstorm tutorial². There are a total of 306 recording electrodes, including 102 MEG magnetometers and 204 MEG planar gradiometers, for which the sampling frequency is 1793 Hz. The length of the signal per trial is 400 ms, and the prestimulus moment is -100 ms to 0 ms. The poststimulus MEG information is recorded in the next 300 ms (0 ms indicates the start of stimulation). We selected 301 samples from the left hand as the experimental data. After data preprocessing based on Brainstorm, we selected the 102 magnetometer channels and intercepted the 250 ms time course starting from 0 ms as the scalp signal. The lead field matrix was calculated based on

²<http://neuroimage.usc.edu/bst/download.php>

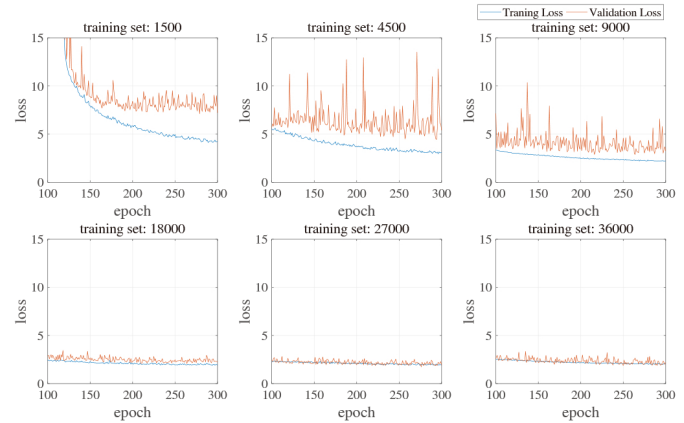


Fig. 13: Results for the training loss and validation loss with various scales of training set. We set the batch-size of optimization for the neural network as 32 and the number of iterations of optimization to 300.

the subject's individual anatomy via the overlapping spheres model [47].

The TBFs of the MEG data were estimated using SEFA, whose components represent a total of 80% of the variance of the signal. To reduce the number of training parameters, we ultimately obtained 48 sampling points after antialiasing filtering and down-sampling. The brain source space was down-sampled to 1024 to facilitate the calculation of the convolutional kernel. The number of spatial components K was set to 3, and the maximum of the source activation area was set to 15 cm^2 . The SNR of the noise block was estimated through prestimulus moment. There were 509,846 parameters in the neural network, and the batch size was set at 32. The

Adam optimization method was selected, in which the learning rate was set as 0.001, hyperparameter β_1 was 0.9, β_2 was 0.999, and ϵ was 10^{-8} . The number of training iterations was set to 300.

Fig. 14 shows the comparison results on the source imaging at 35 ms and 85 ms. Literature studies [48] have shown that the contralateral primary somatosensory cortex (cSI) area exhibits obvious source activation at 35 ms. At 85 ms, the brain source exhibits an obvious activation state in the CSI area and the secondary somatosensory cortex (SII) area, in which the left area of the secondary somatosensory cortices is marked iSII, and the other side is marked cSII. wMNE and LORETA obtain a more diffuse solution in which the activation area is expanded to the motor area. Although SBL and FOCUSS can recover a focal source, a certain spurious source will also appears, and some activation areas are missed. STTONNICA can reconstruct the compact source to a certain extent, locate the cSI area at 35 ms, and recognize the two areas of cSI and cSII at 85 ms, but error is present for the iSII area. Because STTONNICA is sensitive to the initial values of the parameters, many experimental statistical results were required to determine a proper location. Regarding the proposed DAT-DAE, as shown in Fig. 14, the compact activation source in the cSI region can be reconstructed at 35 ms, and DAT-DAE can accurately identify the activation of the CSI and iSII regions at 85 ms. However, since the superior temporal gyrus (STG) region and cSII are very close in spatial structure, this problem increases the difficulty of solving the inverse problem. Many methods tend to reconstruct the STG region, which is exhibited in our experiment and has been proved in previous studies [40]. We find that the proposed DST-DAE tended to reconstruct the STG region.

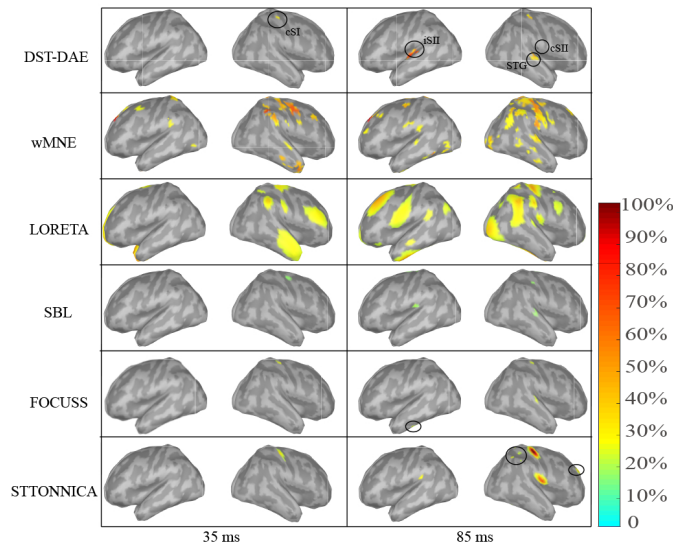


Fig. 14: Comparison of the source imaging of the MEG data at 35 and 85 ms. The MEG median nerve data is from a stimulation experiment on the thumbs. The contralateral primary somatosensory cortex (cSI) area, the secondary somatosensory cortices (SII) area, and the superior temporal gyrus (STG) area are circled in the first row.

IV. DISCUSSION

This paper presents a novel deep learning method, DST-DAE, for estimating the sources of E/MEG recordings. Compared with those of LORETA, wMNE, SBL, FOCUSS, and STTONNICA, the proposed DST-DAE achieves higher detection sensitivity and smaller estimation errors in the source extent, shape and localization in numerical simulation experiments. On the real MEG data, DST-DAE is able to yield a relatively plausible source estimation.

Due to the intrinsic ill-posedness of the ESI problem, prior constraints are essential in knowledge-driven methods to obtain a unique solution. Classical methods include dipole fitting methods [31], [49], L_2 -norm methods [5], [6], sparse-constraint inverse methods [9], [12], and spatio-temporal constraint methods [17], [18]. Traditional dipole fitting methods and sparse-constraint inverse methods, such as FOCUSS and SBL, may fail to accurately identify the extents of sources and tend to estimate a focal source as shown in Fig. 6. On the other hand, the L_2 -norm methods, such as wMNE and LORETA, provide E/MEG source estimates that are too diffuse, and the true activation can easily be mislocalized due to the blurriness of the estimates, as shown in Fig. 4, 6, 8 and 14. For the spatio-temporal constraint methods, STTONNICA achieves better source imaging performance than the sparse and spatial-only constraint methods, but a major challenge is that the inference procedure may be computationally demanding. In addition, STTONNICA solves the ESI problem by combining spatio-temporal information under a nonnegative factorization model, while the model makes the solution sensitive to initialization.

In this paper, we use a data-synthesized deep learning approach to solve the ESI problem. The data synthesis is an effective strategy for introducing prior knowledge without mathematical constraints. Then, with large-scale training, the neural network can automatically extract inverse mapping through synthetic data. Previous studies have suggested that brain activities may be spatially contiguous and locally homogeneous [50]–[52]. To better exploit the spatial properties of data, we incorporate these spatial properties into the data synthesis, which allows the network to produce estimates that are compact with accurate extents. Apart from the spatial information, we further exploit temporal information to enhance the neural network performance via a set of TBFs, in which the component signals are extracted from noisy E/MEG data. In the traditional methods [53], [54], the TBFs are modeled as temporal components of current sources under a probabilistic graphic model. Instead, we use the TBFs as the basis to generate training data with different temporal states. First, the realistic temporal information of recordings is contained by these temporal profiles, so it allows the network to conveniently exploit the temporal information without mathematical modeling. In addition, the different temporal states generated by the TBFs can increase the diversity of the training data within an efficient constraint, preventing difficulty in training due to excessive diversity. Thus, the TBFs can not only increase the generalizability of the neural network but also reduce the complexity of the network training.

SIFNet [28] also utilized a deep learning approach with data generation for the ESI problem, but there are three major differences between SIFNet and DST-DAE: 1) SIFNet only focuses on the single source estimation, while DST-DAE can estimate a multisource case; 2) SIFNet focuses on the source localization by reformulating the ESI problem as a classification problem, while DST-DAE further considers the regression of the temporal dynamics of the estimated sources; 3) SIFNet utilizes training signals corrupted with different SNRs to guarantee a modest denoising ability, leading to more sensitivity to the noise levels of the test samples, while DST-DAE has a superior and efficient denoising ability against different noise levels due to its denoising architecture.

Below, we further discuss the efficacy of the DAE architecture and the time complexity of the deep learning approach. In addition, we explore the limitations of our approach and future directions.

A. Efficacy of the Denoising Autoencoder

Because of the characteristics of the DAE, our network can sensitively extract spatio-temporal features under the condition of high noise. Additionally, the bottleneck structure of the autoencoder helps the network to remove invalid information and extract generalized high-level features. We also experimentally tried to add more noise for denoising training. The experiment shows that architecture based on the DAE can achieve better antinoise ability but will reduce the source localization accuracy. Thus, in practical applications, the denoising ability and the signal reconstruction accuracy can be balanced as needed.

B. Time Complexity of Neural Network

In practice, the batch size of the network was 32, the total number of trainable neuron parameters was 509,846, and the number of training iterations was 300. Given the fixed architecture and hyperparameters, the time complexity depends on the number of training samples, which is $\mathcal{O}(n)$. The mean run-times per epoch for different training sample sizes on a single 12 GB TITAN-Xp GPU are shown in Table III. Furthermore, to measure the prediction time on the trained neural network, we made 100 predictions with real data, and the average prediction time for each dataset is 3.598 ± 0.152 sec.

Training Sample	1500	4500	9000	18000	27000	36000
Time/epoch (s)	9.2	28.8	61.2	125.2	170.2	232.4

TABLE III: Results for mean run-time per epoch in training different sample sizes. the number of training iterations is 300 and the experiment device is a single 12 GB TITAN-Xp GPU.

It can demonstrate that although the neural network method is time-consuming in the training process, the trained neural network can quickly predict new data without tuning hyperparameters. Compared with the traditional method, DST-DAE can achieve a superior performance of recovering source. It only needs the lead field matrix of data, which can be conveniently applied in offline practice.

C. Limitations and Future Directions

At present, a decline occurs in the reconstruction performance for more complex multisource scenarios. There are two reasons for this decline. On the one hand, the difficulty of training the network increases as the complexity of the dataset increases. On the other hand, MSE and MAE are simple but insensitive to the spatial variation of the sources. This causes a vanishing back-propagation gradient for a complex scenario, and then it is easy for the network to fall into local optima. All of these factors will ultimately lead to overfitting, affecting the source estimate performance.

Since the neural network itself has a very large number of parameters, we currently need to downsample the source space for parameter reduction. To reconstruct a high-resolution source space, the neural network method needs to generate more neuron parameters, so more computing power is required. Although DST-DAE uses the BN method to avoid manual adjustment of the initial parameters, tuning each layer's settings will be a time-consuming task as the source resolution increases.

According to the sections III-F and III-G, we reveal that the performance limit is decided by the network architecture and loss function rather than the data scale and loss weight. Therefore, in future work, we will focus on designing a better architecture and a more sensitive loss function for dealing with complex brain source situations.

V. CONCLUSION

In conclusion, we proposed a new data-driven neural method to solve the ESI problem. Compared with the traditional methods, which utilize prior modeling to estimate sources, we generated large-scale training sets via a data synthesis strategy, driving the neural network to automatically learn scalp-to-source mapping. Considering the spatio-temporal characteristics of E/MEG signals, we introduced spatio-temporal prior knowledge in the data generation. This strategy can easily utilize prior information without the requirement of mathematical modeling and can conveniently be applied to a new batch of data without optimizing the parameters again. Furthermore, the architecture of DAE is designed with specific blocks to robustly resist high-level noise and better spatio-temporal feature extraction. Simulation and real data experiments show that DST-DAE not only achieves better brain source reconstruction than the traditional model-driven methods but also offers excellent antinoise performance. Our future work will focus on designing better architecture and loss functions for dealing with complex brain source situations.

REFERENCES

- [1] B. He, L. Yang, C. Wilke, and H. Yuan, "Electrophysiological imaging of brain activity and connectivity—challenges and opportunities," *IEEE Transactions on Biomedical Engineering*, vol. 58, no. 7, pp. 1918–1931, Jul. 2011.
- [2] C. M. Michel, M. M. Murray, G. Lantz, S. Gonzalez, L. Spinelli, and R. G. de Peralta, "EEG source imaging," *Clinical Neurophysiology*, vol. 115, no. 10, pp. 2195–2222, Oct. 2004.
- [3] S. Baillet, J. Mosher, and R. Leahy, "Electromagnetic brain mapping," *IEEE Signal Processing Magazine*, vol. 18, no. 6, pp. 14–30, 2001.

- [4] M. S. Hämäläinen and R. J. Ilmoniemi, "Interpreting magnetic fields of the brain: minimum norm estimates," *Medical & Biological Engineering & Computing*, vol. 32, no. 1, pp. 35–42, Jan. 1994.
- [5] A. M. Dale and M. I. Sereno, "Improved localization of cortical activity by combining EEG and MEG with MRI cortical surface reconstruction: A linear approach," *Journal of Cognitive Neuroscience*, vol. 5, no. 2, pp. 162–176, Apr. 1993.
- [6] R. Pascual-Marqui, C. Michel, and D. Lehmann, "Low resolution electromagnetic tomography: a new method for localizing electrical activity in the brain," *International Journal of Psychophysiology*, vol. 18, no. 1, pp. 49–65, Oct. 1994.
- [7] R. Grech, T. Cassar, J. Muscat, K. P. Camilleri, S. G. Fabri, M. Zervakis, P. Xanthopoulos, V. Sakkalis, and B. Vanrumste, "Review on solving the inverse problem in EEG source analysis," *Journal of NeuroEngineering and Rehabilitation*, vol. 5, no. 1, p. 25, 2008.
- [8] H. Becker, L. Albera, P. Comon, R. Gribonval, F. Wendling, and I. Merlet, "Brain-source imaging: From sparse to tensor models," *IEEE Signal Processing Magazine*, vol. 32, no. 6, pp. 100–112, Nov. 2015.
- [9] I. F. Gorodnitsky, J. S. George, and B. D. Rao, "Neuromagnetic source imaging with FOCUSS: a recursive weighted minimum norm algorithm," *Electroencephalography and Clinical Neurophysiology*, vol. 95, no. 4, pp. 231–251, Oct. 1995.
- [10] L. Ding and B. He, "Sparse source imaging in electroencephalography with accurate field modeling," *Human brain mapping*, vol. 29, no. 9, pp. 1053–1067, 2008.
- [11] P. Xu, Y. Tian, H. Chen, and D. Yao, "Lp norm iterative sparse solution for eeg source localization," *IEEE transactions on biomedical engineering*, vol. 54, no. 3, pp. 400–409, 2007.
- [12] D. Wipf and S. Nagarajan, "A unified bayesian framework for MEG/EEG source imaging," *NeuroImage*, vol. 44, no. 3, pp. 947–966, Feb. 2009.
- [13] D. P. Wipf, J. P. Owen, H. T. Attias, K. Sekihara, and S. S. Nagarajan, "Robust bayesian estimation of the location, orientation, and time course of multiple correlated neural sources using MEG," *NeuroImage*, vol. 49, no. 1, pp. 641–655, Jan. 2010.
- [14] J. P. Owen, D. P. Wipf, H. T. Attias, K. Sekihara, and S. S. Nagarajan, "Performance evaluation of the champagne source reconstruction algorithm on simulated and real m/eeg data," *Neuroimage*, vol. 60, no. 1, pp. 305–323, 2012.
- [15] W. Wu, S. Nagarajan, and Z. Chen, "Bayesian machine learning: Eeg/meg signal processing measurements," *IEEE Signal Processing Magazine*, vol. 33, no. 1, pp. 14–36, 2015.
- [16] C. Cai, M. Diwakar, A. Hashemi, S. Haufe, K. Sekihara, and S. S. Nagarajan, "Robust estimation of noise for electromagnetic brain imaging with the champagne algorithm," *NeuroImage*, p. 117411, 2020.
- [17] K. Liu, Z. L. Yu, W. Wu, Z. Gu, and Y. Li, "Straps: A fully data-driven spatio-temporally regularized algorithm for m/eeg patch source imaging," *International journal of neural systems*, vol. 25, no. 04, p. 1550016, 2015.
- [18] P. A. Valdés-Sosa, M. Vega-Hernández, J. M. Sánchez-Bornot, E. Martínez-Montes, and M. A. Bobes, "EEG source imaging with spatio-temporal tomographic nonnegative independent component analysis," *Human Brain Mapping*, vol. 30, no. 6, pp. 1898–1910, Jun. 2009.
- [19] F. G. Awan, O. Saleem, and A. Kiran, "Recent trends and advances in solving the inverse problem for EEG source localization," *Inverse Problems in Science and Engineering*, vol. 27, no. 11, pp. 1521–1536, Jul. 2018.
- [20] T. R. Knösche, M. Gräser, and A. Anwander, "Prior knowledge on cortex organization in the reconstruction of source current densities from EEG," *NeuroImage*, vol. 67, pp. 7–24, Feb. 2013.
- [21] A. M. Dale, A. K. Liu, B. R. Fischl, R. L. Buckner, J. W. Belliveau, J. D. Lewine, and E. Halgren, "Dynamic statistical parametric mapping," *Neuron*, vol. 26, no. 1, pp. 55–67, Apr. 2000.
- [22] S. Arridge, P. Maass, O. Öktem, and C.-B. Schönlieb, "Solving inverse problems using data-driven models," *Acta Numerica*, vol. 28, pp. 1–174, 2019.
- [23] U. R. Abeyratne, Y. Kinouchi, H. Oki, J. Okada, F. Shichijo, and K. Matsumoto, "Artificial neural networks for source localization in the human brain," *Brain Topography*, vol. 4, no. 1, pp. 3–21, 1991.
- [24] G. Van Hoey, J. De Clercq, B. Vanrumste, R. Van de Walle, I. Lemahieu, M. D'Havé, and P. Boon, "Eeg dipole source localization using artificial neural networks," *Physics in Medicine & Biology*, vol. 45, no. 4, p. 997, 2000.
- [25] M. Yuasa, Q. Zhang, H. Nagashino, and Y. Kinouchi, "Eeg source localization for two dipoles by neural networks," in *Proceedings of the 20th Annual International Conference of the IEEE Engineering in Medicine and Biology Society. Vol. 20 Biomedical Engineering Towards the Year 2000 and Beyond (Cat. No. 98CH36286)*, vol. 4. IEEE, 1998, pp. 2190–2192.
- [26] U. R. Abeyratne, G. Zhang, and P. Saratchandran, "Eeg source localization: a comparative study of classical and neural network methods," *International journal of neural systems*, vol. 11, no. 04, pp. 349–359, 2001.
- [27] I. Goodfellow, Y. Bengio, and A. Courville, *Deep learning*. MIT press, 2016.
- [28] R. Sun, A. Sohrabpour, S. Ye, and B. He, "Sifnet: Electromagnetic source imaging framework using deep neural networks," *bioRxiv*, 2020.
- [29] B. C. Csáji *et al.*, "Approximation with artificial neural networks," *Faculty of Sciences, Eötvös Loránd University, Hungary*, vol. 24, no. 48, p. 7, 2001.
- [30] P. Vincent, H. Larochelle, I. Lajoie, Y. Bengio, P.-A. Manzagol, and L. Bottou, "Stacked denoising autoencoders: Learning useful representations in a deep network with a local denoising criterion," *Journal of machine learning research*, vol. 11, no. 12, 2010.
- [31] B. He, T. Musha, Y. Okamoto, S. Homma, Y. Nakajima, and T. Sato, "Electric dipole tracing in the brain by means of the boundary element method and its accuracy," *IEEE Transactions on Biomedical Engineering*, vol. BME-34, no. 6, pp. 406–414, Jun. 1987.
- [32] M. Hamalainen and J. Sarvas, "Realistic conductivity geometry model of the human head for interpretation of neuromagnetic data," *IEEE Transactions on Biomedical Engineering*, vol. 36, no. 2, pp. 165–171, Feb. 1989.
- [33] R. T. Schirrmester, J. T. Springenberg, L. D. J. Fiederer, M. Glasstetter, K. Eggenberger, M. Tangermann, F. Hutter, W. Burgard, and T. Ball, "Deep learning with convolutional neural networks for brain mapping and decoding of movement-related information from the human eeg," *arxiv*, 2017, *arXiv preprint arXiv:1703.05051*.
- [34] S. Sakhavi, C. Guan, and S. Yan, "Learning temporal information for brain-computer interface using convolutional neural networks," *IEEE Transactions on Neural Networks and Learning Systems*, vol. 29, no. 11, pp. 5619–5629, 2018.
- [35] O. Kwon, M. Lee, C. Guan, and S. Lee, "Subject-independent brain-computer interfaces based on deep convolutional neural networks," *IEEE Transactions on Neural Networks and Learning Systems*, pp. 1–14, 2019.
- [36] A. Odena, V. Dumoulin, and C. Olah, "Deconvolution and checkerboard artifacts," *Distill*, vol. 1, no. 10, p. e3, 2016.
- [37] D.-A. Clevert, T. Unterthiner, and S. Hochreiter, "Fast and accurate deep network learning by exponential linear units (elus)," *arXiv preprint arXiv:1511.07289*, 2015.
- [38] S. Ioffe and C. Szegedy, "Batch normalization: Accelerating deep network training by reducing internal covariate shift," *arXiv preprint arXiv:1502.03167*, 2015.
- [39] S. S. Nagarajan, H. T. Attias, K. E. Hild, and K. Sekihara, "A probabilistic algorithm for robust interference suppression in bioelectromagnetic sensor data," *Statistics in medicine*, vol. 26, no. 21, pp. 3886–3910, 2007.
- [40] W. Ou, M. S. Hämäläinen, and P. Golland, "A distributed spatio-temporal eeg/meg inverse solver," *NeuroImage*, vol. 44, no. 3, pp. 932–946, 2009.
- [41] F. Tadel, S. Baillet, J. C. Mosher, D. Pantazis, and R. M. Leahy, "Brainstorm: a user-friendly application for meg/eeg analysis," *Computational intelligence and neuroscience*, vol. 2011, 2011.
- [42] A. Gramfort, T. Papadopoulos, E. Olivi, and M. Clerc, "Openmeeg: opensource software for quasistatic bioelectromagnetics," *Biomedical engineering online*, vol. 9, no. 1, p. 45, 2010.
- [43] D. P. Kingma and J. Ba, "Adam: A method for stochastic optimization," *arXiv preprint arXiv:1412.6980*, 2014.
- [44] A. Gotmare, N. S. Keskar, C. Xiong, and R. Socher, "A closer look at deep learning heuristics: Learning rate restarts, warmup and distillation," *arXiv preprint arXiv:1810.13243*, 2018.
- [45] D. L. Alexander, A. Tropsha, and D. A. Winkler, "Beware of r²: simple, unambiguous assessment of the prediction accuracy of qsar and qsp models," *Journal of chemical information and modeling*, vol. 55, no. 7, pp. 1316–1322, 2015.
- [46] N. Otsu, "A threshold selection method from gray-level histograms," *IEEE transactions on systems, man, and cybernetics*, vol. 9, no. 1, pp. 62–66, 1979.
- [47] M. Huang, J. C. Mosher, and R. Leahy, "A sensor-weighted overlapping-sphere head model and exhaustive head model comparison for meg," *Physics in Medicine & Biology*, vol. 44, no. 2, p. 423, 1999.
- [48] R. Hari and N. Forss, "Magnetoencephalography in the study of human somatosensory cortical processing," *Philosophical Transactions of the Royal Society of London. Series B: Biological Sciences*, vol. 354, no. 1387, pp. 1145–1154, 1999.

- [49] J. C. Mosher, P. S. Lewis, and R. M. Leahy, "Multiple dipole modeling and localization from spatio-temporal meg data," *IEEE transactions on biomedical engineering*, vol. 39, no. 6, pp. 541–557, 1992.
- [50] M. Hämäläinen, R. Hari, R. J. Ilmoniemi, J. Knuutila, and O. V. Lounasmaa, "Magnetoencephalography—theory, instrumentation, and applications to noninvasive studies of the working human brain," *Reviews of modern Physics*, vol. 65, no. 2, p. 413, 1993.
- [51] J. X. Tao, A. Ray, S. Hawes-Ebersole, and J. S. Ebersole, "Intracranial eeg substrates of scalp eeg interictal spikes," *Epilepsia*, vol. 46, no. 5, pp. 669–676, 2005.
- [52] A. Destexhe, D. Contreras, and M. Steriade, "Spatiotemporal analysis of local field potentials and unit discharges in cat cerebral cortex during natural wake and sleep states," *Journal of Neuroscience*, vol. 19, no. 11, pp. 4595–4608, 1999.
- [53] J. M. Zumer, H. T. Attias, K. Sekihara, and S. S. Nagarajan, "Probabilistic algorithms for meg/eeg source reconstruction using temporal basis functions learned from data," *NeuroImage*, vol. 41, no. 3, pp. 924–940, 2008.
- [54] N. J. Trujillo-Barreto, E. Aubert-Vázquez, and W. D. Penny, "Bayesian m/eeg source reconstruction with spatio-temporal priors," *Neuroimage*, vol. 39, no. 1, pp. 318–335, 2008.

Supplementary Material for "Electromagnetic Source Imaging via a Data-Synthesis-Based Denoising Autoencoder"

Gexin Huang, Zhu Liang Yu*, *Member, IEEE*, Ke Liu, Zheng Hui Gu, *Member, IEEE*, Feifei Qi, Yuanqing Li, *Fellow, IEEE*, Jiawen Liang, and Wei Wu*, *Senior Member, IEEE*,

I. PERFORMANCE METRICS

By letting \mathbf{S} and $\hat{\mathbf{S}}$ denote the simulated and reconstructed sources, respectively, the energies of the simulated and reconstructed sources are $\mathbf{q} = \text{diag}(\mathbf{S}\mathbf{S}^\top)$ and $\hat{\mathbf{q}} = \text{diag}(\hat{\mathbf{S}}\hat{\mathbf{S}}^\top)$. The ij^{th} elements of \mathbf{S} and $\hat{\mathbf{S}}$ (i.e., s_{ij} and \hat{s}_{ij}) denote simulated and estimated i^{th} source at time j^{th} , respectively. The i^{th} elements of \mathbf{q} and $\hat{\mathbf{q}}$ (i.e., q_i and \hat{q}_i) denote simulated and estimated energies of the i^{th} source, respectively.

1) *Area under the receiver operating characteristic (ROC) curve (AUC)*: The AUC evaluates the sensitivity and specificity of the source detection and is derived from the receiver operating characteristic (ROC) curve, which is a graphical plot of the true positive rate (TPR) over the false positive rate (FPR) of the source estimates as the discrimination threshold varies [1]. For a specific β , the TPR and FPR are defined as:

$$\text{TPR}(\beta) = \frac{\text{TP}(\beta)}{\text{TP}(\beta) + \text{FN}(\beta)}, \quad \text{FPR}(\beta) = \frac{\text{FP}(\beta)}{\text{FP}(\beta) + \text{TN}(\beta)}$$

where $\text{TP}(\beta)$, $\text{TN}(\beta)$, $\text{FP}(\beta)$, $\text{FN}(\beta)$ represent the true positive (TP), true negative (TN), false positive (FP), and false negative (FN) values for the threshold β . For definition, dipole source i is (1) a TP, if $q_i \neq 0$ and $\frac{\hat{q}_i}{\max(\hat{\mathbf{q}})} \geq \beta$; (2) a TN, if $q_i = 0$ and $\frac{\hat{q}_i}{\max(\hat{\mathbf{q}})} < \beta$; (3) an FP, if $q_i = 0$ and $\frac{\hat{q}_i}{\max(\hat{\mathbf{q}})} \geq \beta$; (4) an FN, if $q_i \neq 0$ and $\frac{\hat{q}_i}{\max(\hat{\mathbf{q}})} < \beta$.

Because there are considerably fewer active sources ($\sim \mathcal{O}(10^2)$) than inactive sources ($\sim \mathcal{O}(10^3)$), the computed AUC values may be biased. To obtain an unbiased AUC, we repetitively (50 times in our simulations) and randomly sample the same number of inactive dipoles as active dipoles from both close fields and far fields of simulated sources [1]. A larger AUC value indicates that a method has higher detection sensitivity.

2) *Relative mean square error (RMSE)*: For the purpose of evaluating the accuracy of shapes of the reconstructed time courses, we propose the RMSE as the square error between the normalized estimated and simulated sources time courses [2]: $\text{RMSE} = \|\hat{\mathbf{S}}^\dagger - \mathbf{S}^\dagger\|_{\mathcal{F}}^2$, where $\hat{\mathbf{S}}^\dagger = \frac{\hat{\mathbf{S}}}{\|\hat{\mathbf{S}}\|_{\mathcal{F}}}$ and $\mathbf{S}^\dagger = \frac{\mathbf{S}}{\|\mathbf{S}\|_{\mathcal{F}}}$ are the normalized estimated and simulated sources respectively. A lower RMSE value indicates that a method is able to reconstruct the shapes of time courses with a high accuracy.

3) *Spatial dispersion (SD)*: To measure the extent of spatial blurring for the extents of the estimated sources, we introduce SD [3], [4], which is defined as

$$\text{SD} = \sqrt{\frac{\sum_{k=1}^K \sum_{i \in \mathcal{I}_k} d_{ki}^2 \hat{q}_i}{\sum_{i=1}^{d_s} \hat{q}_i}}, \quad \mathcal{I}_k = \{i | k = \arg \min_{k'} d_{k'i}, 1 \leq k' \leq K\}$$

where d_{ki} denotes the distance between the k^{th} dipole and i^{th} dipole, and K is the number of the active dipoles in the simulated map. \mathcal{I}_k is the index set of dipoles in the estimated map, which is spatially closest to the k^{th} active dipole in the simulated map. SD values close to zero indicate that there are no active sources outside the simulated patches. Large SD values may be caused by either sources far from the simulated patches or the spatial spread of the reconstructed sources around the extent of the simulated patches.

4) *Distance of localization error (DLE)*: The DLE is defined as the average distance between the k^{th} true source and the estimated dipole with the maximum energy among the dipoles indexed by \mathcal{I}_k [3], [4]:

$$\text{DLE} = \frac{1}{K_J} \sum_{k \in J} \text{DLE}_k, \quad J = \{k | \mathcal{I}_k \neq \emptyset\}, \quad \text{DLE}_k = \{d_{ki} | i = \arg \max_{i'} \hat{q}_{i'}, i' \in \mathcal{I}_k\}$$

where K_J denotes the number of elements in J , which is the set containing the indices of the detected true sources. DLE_k measures the distance between the k^{th} true source and the estimated source with the maximum energy among the sources indexed by \mathcal{I}_k , and DLE is the average of DLE_k over the true source indices k . A better imaging method is expected to yield a smaller DLE.

5) *Coefficient of determination (R^2)*: To measure the goodness of fit of the neural network model for simulated sources, we calculate the prediction R^2 [5] between estimated and simulated sources, which is defined as

$$R^2 = 1 - \frac{1}{I} \sum_i \frac{\sum_j^J (s_{ij} - \hat{s}_{ij})^2}{\sum_j^J (s_{ij} - \bar{s}_i)^2}, \quad \bar{s}_i = \frac{1}{J} \sum_j s_{ij}, \quad (1)$$

where I and J denotes the number of sources and samples respectively, and R^2 ranges from $-\infty$ to 1. A larger R^2 indicates the neural network shows a better reconstruction performance of sources, and $R^2 = 1$ indicates that the reconstructed sources perfectly fit the simulated sources.

II. DETAILS OF OTSU'S THRESHOLD

To visualize the reconstructed sources at specific time point s_t , we show the absolute value of the reconstructed sources, normalized to its maximum activity, and the threshold is chosen by Otsu's method [1], [6], [7]. Specifically, we divide the normalized source \tilde{s}_t ($\tilde{s}_t = \frac{|s_t|}{\max(|s_t|)}$) into M levels $[1, 2, \dots, M]$. In this paper, M is set to be 100. The number of sources at level i is denoted by n_i and the total number of sources $d_s = \sum_{i=1}^M n_i$. In order to simplify the discussion, the active-level histogram is regarded as a probability distribution:

$$p_i = \frac{n_i}{d_s}, \quad p_i \geq 0, \quad \sum_{i=1}^M p_i = 1 \quad (2)$$

We dichotomize the sources into two classes C_0 and C_1 (active and inactive sources) by a threshold at level k ; C_0 denotes sources with levels $[1, 2, \dots, k]$, and C_1 denotes sources with levels $[k+1, \dots, M]$. Then the probabilities of class occurrence and the class mean levels are given by

$$\begin{aligned} w_0 &= P(C_0) = \sum_{i=1}^k p_i = w(k) \\ w_1 &= P(C_1) = \sum_{i=k+1}^M p_i = 1 - w(k) \end{aligned} \quad (3)$$

and

$$\begin{aligned} \mu_0 &= \sum_{i=1}^k iP(i|C_0) = \sum_{i=1}^k \frac{ip_i}{w_0} = \frac{\mu(k)}{w(k)} \\ \mu_1 &= \sum_{i=k+1}^M iP(i|C_1) = \sum_{i=k+1}^M \frac{ip_i}{w_1} = \frac{\mu_T - \mu(k)}{1 - w(k)} \end{aligned} \quad (4)$$

where $w(k) = \sum_{i=1}^k p_i$ and $\mu(k) = \sum_{i=1}^k ip_i$ are the zeroth- and the first-order cumulative moments of the histogram up to the k th level respectively. $\mu_T = \sum_{i=1}^M ip_i$ denotes the total mean level, and $w_0\mu_0 + w_1\mu_1 = \mu_T$.

In order to evaluate the "goodness" of the threshold at level k , Otsu [7] employed the discriminant criterion measure (or measure of class separability) used in the discriminant analysis:

$$\eta = \frac{\sigma_B^2}{\sigma_T^2} \quad (5)$$

where

$$\begin{aligned} \sigma_B^2 &= w_0(\mu_0 - \mu_T)^2 + w_1(\mu_1 - \mu_T)^2 = w_0w_1(\mu_1 - \mu_0)^2 \\ \sigma_T^2 &= \sum_{i=1}^M (i - \mu_T)^2 p_i \end{aligned} \quad (6)$$

are the between-class variance and the total variances of levels, respectively. Since σ_T^2 is independent of k , the optimal threshold k^* is

$$\sigma_B^2(k^*) = \max_{1 \leq k \leq M} \sigma_B^2(k) = \max_{1 \leq k \leq M} \frac{[\mu_T w(k) - \mu(k)]}{w(k)[1 - w(k)]} \quad (7)$$

Hence, neither the ground truth nor the inverse solutions during the baseline period are required to determine the imaging threshold using Otsu's method. To show the imaging results at a specific time point t , the reconstructed sources at this time point, s_t , is enough to determine the imaging threshold.

REFERENCES

- [1] C. Grova, J. Daunizeau, J.-M. Lina, C. G. Bénar, H. Benali, and J. Gotman, "Evaluation of eeg localization methods using realistic simulations of interictal spikes," *Neuroimage*, vol. 29, no. 3, pp. 734–753, 2006.
- [2] R. A. Chowdhury, Y. Zerouali, T. Hedrich, M. Heers, E. Kobayashi, J.-M. Lina, and C. Grova, "Meg–eeg information fusion and electromagnetic source imaging: from theory to clinical application in epilepsy," *Brain topography*, vol. 28, no. 6, pp. 785–812, 2015.
- [3] W.-T. Chang, A. Nummenmaa, J.-C. Hsieh, and F.-H. Lin, "Spatially sparse source cluster modeling by compressive neuromagnetic tomography," *NeuroImage*, vol. 53, no. 1, pp. 146–160, 2010.
- [4] M. Zhu, W. Zhang, D. L. Dickens, and L. Ding, "Reconstructing spatially extended brain sources via enforcing multiple transform sparseness," *NeuroImage*, vol. 86, pp. 280–293, 2014.
- [5] D. L. Alexander, A. Tropsha, and D. A. Winkler, "Beware of r^2 : simple, unambiguous assessment of the prediction accuracy of qsar and qspr models," *Journal of chemical information and modeling*, vol. 55, no. 7, pp. 1316–1322, 2015.
- [6] R. A. Chowdhury, J. M. Lina, E. Kobayashi, and C. Grova, "Meg source localization of spatially extended generators of epileptic activity: comparing entropic and hierarchical bayesian approaches," *PloS one*, vol. 8, no. 2, p. e55969, 2013.
- [7] N. Otsu, "A threshold selection method from gray-level histograms," *IEEE transactions on systems, man, and cybernetics*, vol. 9, no. 1, pp. 62–66, 1979.